

Mapping the Surface of the Magnetar 1E 1048.1–5937 in Outburst and Quiescence Through Phase Resolved X-ray Spectroscopy

Tolga Güver¹, Ersin Göğüş² & Feryal Özel³

¹ *Istanbul University, Science Faculty, Department of Astronomy and Space Sciences, Beyazıt, 34119, Istanbul, Turkey*

² *Sabancı University, Faculty of Engineering and Natural Sciences, Orhanlı Tuzla 34956 Istanbul Turkey*

³ *Department of Astronomy, University of Arizona, 933 N. Cherry Ave., Tucson, AZ 85721*

ABSTRACT

We model the pulse profiles and the phase resolved spectra of the anomalous X-ray pulsar 1E 1048.1–5937 obtained with XMM-Newton to map its surface temperature distribution during an active and a quiescent epoch. We develop and apply a model that takes into account the relevant physical and geometrical effects on the neutron star surface, magnetosphere, and spacetime. Using this model, we determine the observables at infinity as a function of pulse phase for different numbers and sizes of hot spots on the surface. We show that the pulse profiles extracted from both observations can be modeled with a single hot spot and an antipodal cool component. The size of the hot spot changes from $\approx 80^\circ$ in 2007, 3 months after the onset of a dramatic flux increase, to $\approx 30^\circ$ during the quiescent observation in 2011, when the pulsed fraction returned to the pre-outburst $\approx 65\%$ level. For the 2007 observation, we also find that a model consisting of a single 0.4 keV hot spot with a magnetic field strength of 1.8×10^{14} G accounts for the spectra obtained at three different pulse phases but underpredicts the flux at the pulse minimum, where the contribution to the emission from the cooler component is non-negligible. The inferred temperature of the spot stays approximately constant between different pulse phases, in agreement with a uniform temperature, single hot spot model. These results suggest that the emitting area grows significantly during outbursts but returns to its persistent and significantly smaller size within a few year timescale.

Subject headings: stars: neutron — X-rays: 1E 1048.1–5937

1. Introduction

Multiwavelength observations and monitoring campaigns in the past decade revealed a large number of fundamental characteristics of Anomalous X-ray Pulsars (AXPs) and Soft-Gamma Repeaters (SGRs). There is strong evidence in favor of very high neutron star magnetic field strengths,

obtained from observations of their rates of spindown, their ultra-energetic bursts, and their high persistent X-ray luminosities (see, e.g., Woods & Thompson 2006 and Mereghetti 2008 for detailed reviews). Indeed, the magnetar model (Thompson & Duncan 1995), in which a magnetic field in excess of $B \sim \text{few} \times 10^{13}$ G is responsible for powering the persistent emission and giving rise to the bursting activity, has been successful in explaining a wide variety of broad properties of these sources¹.

Despite the significant progress in understanding the basic characteristics of AXPs and SGRs, a number of outstanding questions remain that are related to the properties of their magnetic fields and of their long-term emission. For example, AXPs and SGRs generally exhibit high spindown rates, which indicate high inferred dipole magnetic fields for their typical spin periods in the range of 2–12 s. However, recently a number of radio pulsars with high spindown rates that do not behave like magnetars have been discovered. Conversely, some AXPs that possess low rates of spindown but show magnetar-like behavior have also been observed (see, e.g., Rea et al. 2010, 2012, 2014; Zhou et al. 2014). Even though the magnetic field geometry is thought to play a role in shaping the broadband emission characteristics of AXPs and SGRs (e.g., Güver et al. 2011; Tiengo et al. 2013), there have been no direct probes of their field strength and its variation at the surface.

Second, these sources show a variety of transient phenomena, such as bursts, flares, outbursts, as well as significant changes in their persistent fluxes (see, e.g., Kaspi 2007; Rea & Esposito 2011). It is unclear what the different triggers for these events are, whether the same triggers recur, and what properties of the neutron stars change during the transient events. For example, in one interpretation, a change in the magnetospheric twist angle causes the outbursts, with accompanying spectral changes (Thompson et al. 2007). In a different model, Özel & Güver (2007) attribute the outbursts and post-burst flux enhancements to purely thermal changes in the surface, without any modification to the magnetosphere.

Third, the observed pulsed emission exhibits a variety of pulse morphologies and amplitudes for different sources (e.g., Gavriil & Kaspi 2002). While the gross characteristics of these morphologies can be understood within the context of surface emission from a magnetar (e.g., Özel 2002), pulse-phase-dependent observables, such as the size of the emitting region, its inclination angle, or the compactness of the neutron star, have not been studied in detail and in connection with the global neutron star properties.

One approach toward addressing these questions is by mapping the strength of the magnetic field and the temperature distribution at the neutron star surface through pulse-phase resolved spectroscopy, which is a technique that allows tracking spectral changes as a function of the rotational phase. Mapping these two parameters can, in principle, reveal the number, size, and location of the X-ray emitting regions and help understand the observed pulse shapes. Furthermore, ob-

¹See the online AXP/SGR catalog at <http://www.physics.mcgill.ca/pulsar/magnetar/main.html> for a summary of their properties. (Olausen & Kaspi 2014)

taining the distribution of these parameters on the stellar surface, following their evolution during transient events, and comparing them between different transient phenomena may also provide better insight into the nature of these sources and the underlying physical mechanisms for these events (see, e.g., An et al. 2013; Scholz & Kaspi 2011; Ng et al. 2011; Güver et al. 2007).

In this paper, we analyze the pulse-phase resolved spectra of 1E 1048.1–5937 obtained with XMM-Newton in 2007 and 2011, when it was in outburst and in quiescence, respectively. 1E 1048.1–5937 is a good target for such a study because of its highly active history and its fairly high pulsed fraction, which has been observed to show significant variations over time. 1E 1048.1–5937 was discovered by Seward et al. (1982) with the *Einstein* satellite and is located at a distance of ≈ 9 kpc (Durant & van Kerwijk 2006). Its lowest observed quiescent flux is $\sim 4 - 5 \times 10^{-12}$ erg cm $^{-2}$ s $^{-1}$ (see, e.g., Oosterbroek et al. 1998; Tam et al. 2008; and the discussion below). Observations with *EXOSAT* revealed a spin period of 6.44 s and a pulsed fraction, i.e., the ratio of pulsed flux to total flux, of 65% (Seward et al. 1986). This pulsed fraction is one of the largest among all known AXPs and SGRs, indicating a high degree of localization of the hot region on the surface, which produces the observed pulsed soft X-ray emission as the star rotates.

1E 1048.1–5937 has indeed been one of the most active and variable AXPs since its discovery, showing bursts, outbursts, and significant changes in its quiescent flux. Oosterbroek et al. (1998) reported factor of 4 flux variations over a time span of two decades. In the Rossi X-ray Timing Explorer (RXTE) era, 1E 1048.1–5937 was monitored regularly (see, e.g., Kaspi et al. 2001; Dib, Kaspi & Gavriil 2009). This monitoring campaign resulted in the detection of SGR-like short bursts from an AXP for the first time (Gavriil, Kaspi, & Woods 2002). Accompanying these bursts, 1E 1048.1–5937 also showed outbursts in its pulsed flux in 2003 and 2004 (Gavriil & Kaspi 2004; Gavriil et al. 2006). Finally, it became active again in 2007, showing a large spin-up glitch, which is a sudden increase in its rotation frequency (Dib et al. 2009). X-ray observations with imaging instruments revealed that, while the total flux was seven times greater compared to the quiescent levels, the pulsed fraction decreased from $\approx 70\%$ to $\approx 30\%$ (Tam et al. 2008). This anti-correlation between the total flux and the pulsed fraction was also reported earlier for this source (see, e.g., Tiengo et al. 2005).

The first phase-resolved spectral analysis of 1E 1048.1–5937 was performed by Oosterbroek et al. (1998) using BeppoSAX data; however, due to the low count rates, they were unable to detect any significant phase dependence in the spectral parameters. Later, using a relatively short (≈ 8 ks) XMM-Newton observation performed in 2000, Tiengo et al. (2002) reported that the spectral parameters obtained from phase integrated analysis can describe most of the phase resolved data satisfactorily, with the only variation seen in the overall normalization, which is proportional to the source flux. They found a significant spectral variation only during the phase interval corresponding to the minimum flux. Pulse profile modeling and pulse-phase resolved spectroscopy of other AXPs and SGRs have also been performed in the past using phenomenological models of the surface and magnetospheric emission (see, e.g., Albano et al. 2010; Bernardini et al. 2011). In particular, Albano et al. (2010) analyzed X-ray data of XTE J1810–197 and CXOU J164710.2–455216

using a model that assumes a globally twisted magnetosphere as presented by Nobili, Turolla, & Zane (2008). Their results suggest that during outbursts, a limited fraction of the stellar surface that is close to the magnetic poles is heated and that the subsequent spectral evolution is due to the cooling and the changes in the size of this region.

In this paper, we extend these earlier studies and model pulse-phase resolved spectra of 1E 1048.1–5937 using a physical model that accounts for radiative processes in a strong magnetic field for the persistent emission from a magnetar. In this model, we determine the observables as a function of pulse phase by calculating the emission from the magnetic neutron star atmosphere, transporting this emission through its magnetosphere, and accounting for the general relativistic light bending the photons experience in the strong gravitational field as they travel toward a distant observer. In this first study, we work within the framework of a simple temperature and magnetic field configuration on the stellar surface, where the emission comes from a single or two antipodal hot regions of uniform temperature T and uniform magnetic field B . When modeling pulse profiles, we also take into account the emission from an antipodal cool component originating from the rest of the surface. However, for phase-resolved spectroscopy, we focus on the properties of the active hot spot and neglect the contribution from this dim component.

In Section 2, we discuss the details of the spectral model. In Section 3 we describe the XMM data, while in Section 4 we present the results from the analysis of pulse profiles and the phase resolved spectroscopy. Finally, in Section 5, we discuss the implications of our results.

2. Phase-Resolved Spectral Models of Magnetar Emission

The observed energy and pulse phase distribution of X-ray photons emitted from a magnetar are shaped by a number of processes (see, e.g., Özel 2013). Photons propagate outward from the deeper layers of the stellar crust through an atmosphere in radiative equilibrium characterized by an effective temperature T and a magnetic field strength B . In the case of magnetars, the atmosphere is strongly magnetic ($> 10^{13}$ G) and is expected to consist of a nearly fully ionized electron-proton plasma (Zavlin, Pavlov, Shibano 1996; Özel 2001; Ho & Lai 2001; see also Ho et al. 2003 for partially ionized cases). The strong magnetic field affects the transport of radiation in this plasma significantly: it distorts the spectrum away from a blackbody and causes absorption like features in the X-ray spectra due either to ion cyclotron lines or to the polarization of the vacuum itself (Özel 2001, 2003; Ho & Lai 2003). The polarization-dependent transport in the local magnetic field also determines the beaming of the radiation emerging from the surface.

To model the spectrum and beaming of the surface emission, we use the atmosphere calculations performed by Özel (2001, 2003) at different effective temperatures and magnetic field strengths, assuming a plane parallel atmosphere and a magnetic field vector that is locally perpendicular to the surface. This assumption about the magnetic field geometry is appropriate for emission originating from a highly localized region on the stellar surface, such as a magnetic pole, and allows

us to avoid the immense additional computational cost that is introduced by the additional angle that would otherwise have been required to specify the local direction of the magnetic field, and the second additional angle we would need to consider in the radiative transfer equation when the azimuthal symmetry around the surface normal is broken in this configuration. When the emitting region is a more substantial fraction of the surface, the magnetic field may be inclined with respect to the surface normal and vary in magnitude at different latitudes. Model atmosphere calculations for inclined magnetic fields show that, for larger field inclinations, the spectra emerging from the surface are somewhat softer at photon energies significantly above the peak of the spectrum (see Figure 10 of Lloyd 2003). The model spectra at these higher energies, however, are dominated by resonant scattering in the magnetar magnetosphere (see below), and therefore, ignoring the effects of the inclined magnetic fields does not introduce a large correction to the models.

The interaction of the photons emitted from the surface with the charged particles in the magnetosphere further shapes the observed spectrum. In magnetars, the magnetosphere is expected to be populated by energetic charged particles with a density that exceeds the typical Goldreich-Julian density by many orders of magnitude (Thompson et al. 2002). The energy distribution of surface photons, therefore, gets modified through resonant cyclotron scattering processes off of these charges (e.g., Lyutikov & Gavriil 2006; Fernandez & Thompson 2007) as they pass through the magnetosphere. We take into account the scattering of the thermal photons from the surface in the magnetosphere using the Schwarzschild-Schuster method for solving the radiative transfer equation and angle averaged scattering cross sections, as in the method followed by Lyutikov & Gavriil (2006; see Fernandez & Thompson 2007 for a fully 3D treatment). In this setup, the effect of the magnetospheric scattering on the spectrum is captured by means of two parameters: the total scattering optical depth τ and the average velocity of the electrons in the magnetosphere β , where the latter is defined in units of the speed of light.

Finally, we take into account the effects of gravitational lensing and redshift to calculate the observables at infinity. Because AXPs and SGRs spin very slowly, we use the Schwarzschild metric to describe the neutron star spacetime and follow the method described in Pechenick et al. (1983) to compute spectra at different pulse phases (see Özel 2002 for a detailed description of the algorithm). Gravitational lensing significantly alters the observed pulsed fractions and causes them to be smaller compared to the Newtonian case, since it causes more of the stellar surface to be observable (see, e.g., Pechenick et al. 1983; Psaltis et al. 2000). As in Özel (2002), we assume that there is either a single hot spot or two antipodal hot spots of the same size that are described by a uniform temperature. We also assume that the rest of the neutron star does not radiate in the X-ray band. Thus, in this setup, three geometric parameters determine the flux and spectrum of photons that are observed as a function of spin phase, in addition to the neutron star compactness GM/Rc^2 (see also Zavlin & Pavlov 2002). As shown in Figure 1, these are: (i) the sizes of the hot spots emitting in the X-rays on the surface of the neutron star ρ , (ii) the colatitude of the center of the hot spot with respect to the stellar spin axis, θ_s , and (iii) the observer’s inclination with respect to the stellar spin axis, θ_0 .

Accounting for the physics of the atmosphere, the magnetosphere, and the gravitational lensing, even in a simplified geometry, requires a total of eight parameters ($B, T, \tau, \beta, \rho, \theta_s, \theta_0, GM/Rc^2$), as defined above. In principle, models that incorporate all of these effects should be fit simultaneously to the observed data to constrain the magnetic field strength and temperature distribution on the surface of a magnetar. In reality, however, sampling this parameter space even with a very coarse resolution that corresponds to 10 values for each parameter results in 10^8 models, each of which yields the observed intensity at 64 values of the photon energy (for a relatively coarse energy resolution) and at each of the 30 pulse phases we use in the calculation. In order to reduce the computational requirements of modeling the pulse-phase resolved spectra of magnetars, we follow the approach outlined below.

For slowly spinning neutron stars, there is a near degeneracy in the predicted pulse profiles between changing the compactness of the star and the size of the hot spot: the same pulse amplitude can be achieved with a large compactness and a small spot size or a small compactness and a large spot size. In the analyses presented here, we fix the compactness by assuming representative values for the neutron star mass, $M=1.4 M_\odot$, and radius, $R = 10$ km.

We then use the extraordinarily large pulse amplitude exhibited by 1E 1048.1–5937 at some epochs to place constraints on the geometric parameters of the model, which are not expected to evolve significantly with time. As discussed in Özel et al. (2001), an amplitude as large as 75% can be achieved with a single hot spot and only if one of the two angles θ_s or θ_0 is close to 90° . Moreover, at these small spin frequencies, the pulse amplitude is primarily determined by the product $\sin \theta_s \sin \theta_0$ (Poutanen & Beloborodov 2006), leading to a degeneracy between these two parameters. For this reason, we fix one of the two angles, θ_s , to be 90° . We will further discuss the validity of this assumption in Section 4.1.

Having fixed the compactness of the neutron star and having obtained an estimate of some of the geometric parameters of the model, we then produce a fine grid of theoretical models over a wide range of effective temperatures, magnetic field strengths, as well as optical depths and the average velocities of the charges in the magnetosphere. This computation resulted in an XSPEC compatible additive table model, which is a version of the Surface Thermal Emission and Magnetospheric Scattering model (STEMS, Güver et al. 2007, 2008), where the proper geometric and beaming effects that are necessary for a phase resolved spectral analysis are taken into account. We used this model to perform a formal χ^2 fitting of the phase-resolved X-ray spectra in Section 4.3.

3. Observations & Data Analysis

1E 1048.1–5937 has been observed seven times with XMM-Newton. In this paper, we focus on the observations that were long enough to accumulate sufficient number of source counts for phase resolved spectroscopy and that took place at epochs separated by a sufficiently long period of time to allow us to track its long-term flux evolution following a transient event. There are two such

observations in the archive. The first observation was roughly within three months after a timing glitch event observed in 2007 and two months after the detection of a short SGR-like burst. A simple blackbody plus a power-law fit to the X-ray spectrum extracted from this observation yields an unabsorbed bolometric flux $F = (2.75 \pm 0.02) \times 10^{-11}$ erg s⁻¹ cm⁻², in the 2–10 keV range. The second observation was in 2011, approximately 4 years after this event. The X-ray spectrum extracted from this latter observation yields an unabsorbed flux $F = (4.46 \pm 0.05) \times 10^{-12}$ erg cm⁻² s⁻¹, using, again, a blackbody plus power-law model. This flux is a factor of ≈ 6 smaller than that in outburst, and is similar to the pre-outburst flux reported by Tiengo et al. (2002), at $F = 4.3 \times 10^{-12}$ erg cm⁻² s⁻¹ in the same energy range, and is also one of the lowest fluxes reported for this source (Oosterbroek et al. 1998). We, therefore, conclude that 1E 1048.1–5937 returned to a quiescent state at the time of the 2011 observation, which is further supported by the fact that no activity has been reported since the 2007 event. We show in Table 1 the details of XMM-Newton observations used in this study.

Our initial intent was to use both observations for time-resolved spectroscopy. However, the high energy particle background showed continuous and significant variations throughout the second observation. Eliminating the segments when the background was high and variable results in an exposure time of ≈ 20 ks. Together with the very low source count rate in quiescence, this prevents us from using these data for phase resolved spectral analysis. Therefore, we present our results from the timing analysis for both observations but only perform phase resolved X-ray spectral analysis on the 2007 data.

Both observations were calibrated using the Science Analysis Software (SAS) version 11.0.0 and the latest calibration files as of February 2012. Barycentric correction was applied to the cleaned event files using the *barycen* tool. Source event files were extracted from a circular region centered on the source with a radius of 32 arcseconds. Similar sized background regions were extracted from source free regions of the EPIC pn detector. Given the significantly lower effective areas of the MOS detectors and the known systematic difference in the flux measurements between the pn and MOS detectors², we opted not to use the MOS data. We present below the results from the timing and spectral analysis on these data.

For the phase resolved spectroscopy, we used the SAS tool *phasecalc* to compute the spin phase of each event. In order to best capture the intrinsic structure, while considering count rate limitations, we generated phase resolved spectra by accumulating all events corresponding to the spin phase intervals of 0.0–0.4, 0.4–0.6, 0.6–0.8, and 0.8–1.0. The average number of source counts for each interval were ≈ 58000 , 54000, 65000, and 44000, respectively. These intervals represent the minimum, rise, peak, and the decay of the pulse profile as shown in Figure 2.

For each X-ray spectrum, the corresponding response and ancillary response files were created using the *rmfgen* and *arfgen* tools. All X-ray spectra were grouped to have at least 25 counts in

²<http://xmm2.esac.esa.int/docs/documents/CAL-TN-0018.pdf>

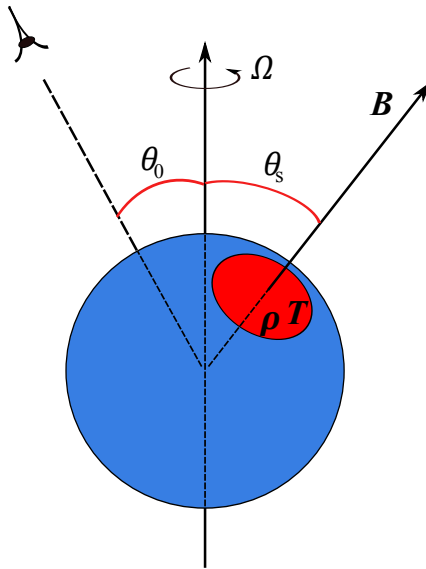


Fig. 1.— A schematic view of a neutron star with one emitting hot spot on the surface. The angle between the rotation and magnetic axis is shown with θ_s and the angle between the rotation axis and the observer is shown with θ_0 . T , B , and ρ denote the temperature, magnetic field strength and the size of the spot, respectively.

Table 1: XMM-Newton Observations of the 1E 1048.1–5937 used in this study.

Observation Name	Date	Observation ID	Exposure (ks)
Obs1	2007-06-14	0510010601	48.91
Obs2	2011-08-06	0654870101	96.92

each energy bin and not to oversample the instrumental energy resolution more than a factor of three, using the *specgroup* tool. During the spectral fits, we added a 2% systematic uncertainty to the data, which represents the current uncertainty in the calibration of the EPIC-pn instrument².

4. Results

4.1. Timing Analysis

We used a Z_m^2 test (Buccheri et al. 1983) with a harmonic number $m = 1$ to search for a periodic signal from 1E 1048.1–5937. We find very prominent signals at frequencies of 0.15484743(3) and 0.15478524(1) Hz for Obs1 and Obs2, respectively.

To investigate the energy dependence of the observed pulse profile and of the pulsed fraction, we generated pulse profiles in the 0.5–1.8 keV, 1.8–3.5 keV, and 3.5–7.0 keV energy bands by folding the lightcurves in these energy ranges at the frequencies measured for each epoch. We chose the above energy ranges to capture the characteristics of the emission in the softer and harder X-ray bands as well as to keep the total number of counts in each band as similar as possible. We show these profiles in the top panels of Figures 3 and 4. Even though the overall structures of pulse profiles in the three energy bands resemble each other, there are discernible differences between them. In particular, the flux (count rate) steadily declines prior to the pulse minimum and increases after that in the lower two energy bands of Obs1, while there is a plateau in the pulse minimum in all energy bands of Obs2.

We computed the phase dependent hardness ratios in order to quantify the dependence of the pulse profiles on photon energy. We define the hardness ratio HR1 as the ratio of counts per bin in the 1.8–3.5 keV to those in the 0.5–1.8 keV band, HR2 as the ratio of counts in the 3.5–7.0 keV to 0.5–1.8 keV band, and HR3 as the ratio of counts in the 3.5–7.0 keV to 1.8–3.5 keV band. We show the phase dependence of hardness ratios in the lower three panels of Figures 3 and 4 from Obs1 and Obs2, respectively. We find that HR3 shows the least amount of variation over the spin phase during both observations. On the other hand, we find clear evidence of spectral variations over the spin phase below 1.8 keV: HR1 and HR2 are systematically above the average hardness in the phase interval ϕ of 0.4–0.8, and below the mean between $\phi \sim 0.9$ –1.2. In other words, the spectrum during the peak of its pulse phase is somewhat harder than that in the minimum during Obs1 and Obs2.

We calculated the root-mean-square (rms) pulsed fractions in the energy bands described above, using the Fourier based method described by van der Klis (1989) and applied by Woods et al. (2004) and Tam et al. (2008), on 1E 2259+586 and 1E 1048.1–5937, respectively. We also calculated it in the 2–10 keV band, where we can directly compare our results with those of Tam et al. 2008 on data obtained with the Chandra X-ray Observatory as 1E 1048.1–5937 went from quiescence in 2006 and to outburst in 2007.

We list the pulsed fractions in all energy bands in Table 2. We find that the rms pulsed fraction increases with photon energy in both observations. In addition, we find that the rms pulsed fraction increased by nearly a factor two when going from the active to the quiescent epoch. The pulsed fractions in all energy bands are anti-correlated with the bolometric flux, attaining the higher values when the flux is lower. The observed trend is very similar (but in the reverse direction) to the one reported by Tam et al. (2008), where the flux increased from $\sim 5 \times 10^{-12}$ to $\sim 4 \times 10^{-11}$ erg s $^{-1}$ cm $^{-2}$, while the pulsed fraction decreased from 0.7 to 0.3 as the source went into outburst (see Table 1 of Tam et al. 2008).

4.2. Phase Averaged Spectral Analysis and Pulse Profile Modelling

We first analyzed the phase-averaged X-ray spectrum extracted from the 2007 XMM-*Newton* observation (see Table 1) to determine the average spectral parameters. Using the phase-averaged STEMS model (Güver et al. 2007, 2008), we obtained a very good fit ($\chi^2/\text{dof} = 0.93$) for a surface temperature $T = 0.4 \pm 0.03$ keV and a magnetic field strength of $B = (1.63 \pm 0.11) \times 10^{14}$ G, where the quoted errors are purely statistical and do not reflect possible systematic errors or biases arising from the assumption of uniform temperature or magnetic field strength across the hot spot in the models. We also performed a fit to the phase averaged spectrum obtained from the 2011 data and found best fit parameter values to be $T = 0.35 \pm 0.03$ keV and $B = (2.51 \pm 0.2) \times 10^{14}$ G, with a $\chi^2/\text{dof} = 1.48$. The statistical quality of this fit is poor because of the high energy particle background during this observation, which could not be properly accounted for. In particular, even after carefully removing the particle background using the *espfilt* tool, the resulting X-ray spectrum still had narrow residual features at around 1 keV and 2 keV regions, which cannot be accounted for by the continuum models. Modeling these features with additional Gaussian components significantly reduced the χ^2/dof but did not affect the resulting fit parameters. Comparing the phase-averaged fits in the outburst and quiescent phases, we note that the temperatures we obtained do not differ significantly from one another despite the large change in the observed flux.

We used the values of the temperature and magnetic field strength obtained from the 2007 observation to generate bolometric pulse profile models. We compare these models to the observed pulse profiles in order to determine the size of the hot spot in the two epochs as well as the angles θ_s and θ_0 . We show in Figure 5 the observed 0.5 – 7.0 keV pulse profiles at the two epochs along with a few representative models covering a range of geometric parameters. For clarity, each profile is normalized to its peak value and the pulse peak is moved to phase 0.0. In the model profiles, we fix one of the angles (specifically, the spot colatitude) at 90° owing to the large pulse amplitudes and because the pulsed fraction depends only on the product of the sine of the two angles, as discussed in Section 2. We then estimate the number and size of the hot spots as well as the observer’s inclination through a comparison with the observed pulse profiles (note that due to the simplicity of the model geometry, we do not perform a formal fit). It is immediately clear from this figure that a configuration with two antipodal hot spots (shown in the long-dashed line) has the wrong

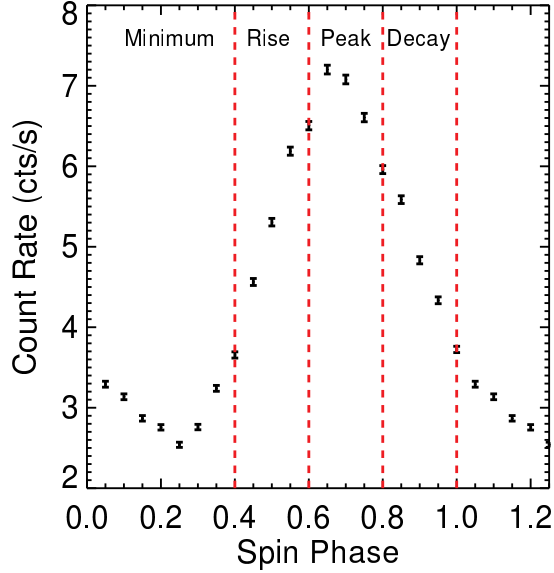


Fig. 2.— Pulse profile extracted from the 2007 observation in the 2.0–10.0 keV band is shown. Vertical dashed lines show the intervals selected for the phase resolved spectroscopy.

Table 2: RMS pulsed fractions for different photon energy ranges*.

Observation Name	Pulsed Fraction			
	0.5 – 1.8 keV	1.8 – 3.5 keV	3.5 – 7.0 keV	2.0 – 10.0 keV
Obs1	0.311(3)	0.350(3)	0.362(5)	0.355(3)
Obs2	0.520(5)	0.633(6)	0.668(11)	0.648(6)

* Values in parenthesis are 1σ uncertainties in the corresponding digit(s) of the measurements.

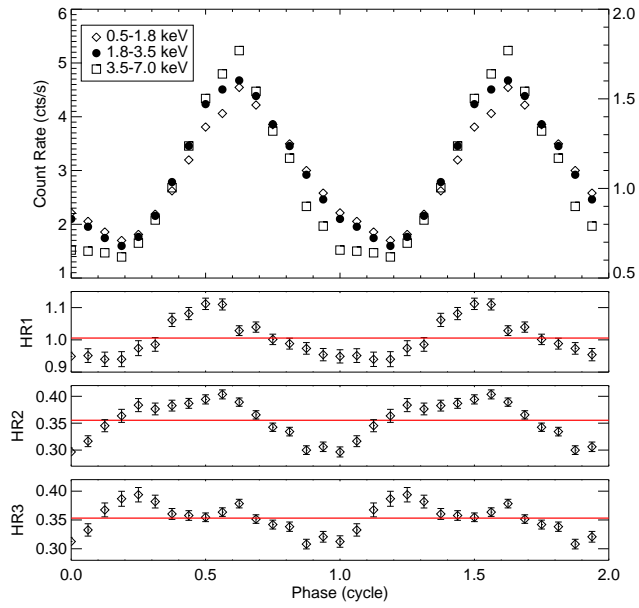


Fig. 3.— *Top Panel:* Pulse profile and its energy dependence during the observation in 2007. The diamond, filled circle, and square symbols show the count rates at 0.5–1.8, 1.8–3.5, and 3.5–7.0 keV energy ranges, respectively. Left axis shows the count rate range for 0.5–1.8 and 1.8–3.5 keV bands while the right axis shows the count-rate range for the 3.5–7.0 keV band. Lower panels show the hardness ratios for different energy ranges as defined in the text. Horizontal red lines show the average hardness values.

number of peaks and cannot even qualitatively describe the observed profiles. In contrast, a single hot spot, with a colatitude of 90° and an observer’s inclination of 45° results in a reasonable match to the observed pulse amplitude (see the discussion below for the pulse minimum).

The spot sizes we obtain for two epochs are significantly different: the pulse profile extracted from the 2007 observation can be reproduced with a spot size $\rho \approx 80^\circ$, while the one in 2011 can be reproduced with a spot size of $\rho \approx 30^\circ$. The resulting difference implies an $\approx 85\%$ decrease in the emitting area from outburst back into quiescence. This is in agreement with expectations from a model where the outburst is caused by thermal changes on the neutron star surface, where the shrinking hot spot size during the decline simultaneously accounts for the observed increase in the pulsed fraction and the decrease in the X-ray flux. We use these results to fix the three geometric parameters in the subsequent analysis of the phase-resolved spectra in Section 4.3.

While the model profiles describe the observed pulse shapes well at the peak and decay pulse phases, they underpredict the flux at pulse minima. This behavior is most likely related to our assumption that the stellar surface outside of a localized hot region is dark and does not contribute at all to the emission. In reality, it is highly likely that the rest of the surface, which is cooler and covers a larger area, also has a small contribution to the observed emission and may become most visible at the pulse minimum, when the hot spot is half a spin phase away from the observer’s line-of-sight. To test this interpretation, we calculated models where we added a large antipodal cool component, but kept all the parameters describing the magnetic field strength, the size, and the geometry of the hot spot the same. We show in Figure 6 the resulting pulse profiles that include a cool spot with an angular size $\rho = 80^\circ$ and a temperature of $T = 0.2$ keV and 0.15 keV, respectively, for the 2007 and 2011 observations. This additional component indeed helps provide a better match to the flux at the pulse minimum. Because we are interested in the characteristics of the hot, active region and the changes to these characteristics between the quiescent and outburst epochs, we do not consider the contribution from this cool component in the rest of the analyses in this paper.

4.3. Phase Resolved Spectral Analysis

We showed in Section 4.1 that the flux observed from 1E 1048.1–5937 depends significantly on the pulse phase. Equivalently, the observed pulse shapes show a strong energy dependence and a significant change between the two observations. To understand in more detail the causes of the phase dependent flux modulations and to assess if these modulations can be used to constrain the magnetic field strength and temperature distribution, we carry out in this section phase resolved X-ray spectroscopy using the model described Section 2.

We fit the spectra obtained at different pulse phases simultaneously, linking only the hydrogen column density and the magnetospheric parameters β and τ between spin phase intervals, since these parameters are not expected to vary throughout the neutron star spin. We obtained a fit

with $\chi^2/\text{dof} = 1.07$ for 477 degrees of freedom. We list the parameters obtained in each phase in Table 3 and show the best-fit models and residuals in Figure 7. We also plot in Figure 8 the spin phase evolution of the best fit parameters.

Overall, we find that a model consisting of a rotating hot spot with a size of 80° and a temperature of ≈ 0.4 keV provides a good fit to the data at all spin phases (but see the next section for a discussion of the pulse minimum). We obtain an average magnetic field strength of 1.8×10^{14} G. The best fit magnetic field strength shows a 13% rms variation as a function of spin phase, which is only at a $2\text{-}\sigma$ level given the statistical uncertainties. Variations of this magnitude are expected given the simplifications in the model, such as the assumption that the magnetic field is uniform throughout the emitting region. We also find a best-fit magnetospheric optical depth $\tau = 4.86 \pm 0.17$ and an average particle velocity $\beta = 0.300 \pm 0.005$. Rea et al. (2008) modeled the same observation using a resonant cyclotron scattering model, where a blackbody spectrum is modified through resonant cyclotron scattering by charges in the neutron star magnetosphere. They reported the magnetospheric parameters as $\tau = 4.7 \pm 0.2$ and $\beta = 0.29 \pm 0.05$, in very good agreement with the results we found here.

5. Discussion

In this paper, we investigated the pulse profile and pulse phase resolved X-ray spectra of 1E 1048.1–5937 to map its surface temperature and measure its magnetic field in outburst and in quiescence. We fit two epochs of XMM data using a spectral model that takes into account the relevant physical and geometrical effects that includes: (i) a strongly magnetized fully ionized hydrogen atmosphere on the neutron star surface characterized by an effective temperature T and a magnetic field strength B and yields the energy distribution and beaming of the emitted photons, (ii) the scattering of these surface photons in the magnetosphere due to the existence of a dense charged particle cloud with a total scattering optical depth τ and an average electron velocity β , (iii) the effects of gravitational lensing and redshift for a slowly rotating neutron star to determine the observables at infinity. These calculations also account for the number and size of the hot spots on the surface, the inclination of the observer’s line-of-sight and the colatitude of the hot spot with respect to the stellar spin axis.

The high pulsed fraction of 1E 1048.1–5937 allows us to constrain the number of the hot spots on the surface to one, the colatitude of the spot to $\theta_s \approx 90^\circ$, and the observer’s inclination to $\theta_0 \approx 45^\circ$. Note that, because these two parameters are degenerate as discussed in Section 2, a configuration with $\theta_s \approx 45^\circ$ and $\theta_0 \approx 90^\circ$ is also equally likely. Furthermore, using the spectral parameters found from the phase averaged spectrum obtained in 2007 and assuming that the angle between the rotation axis and the observer to be $\approx 45^\circ$, we show that the pulse profiles are best described by models where the angular sizes of the hot active region are 80° in 2007 and 30° in 2011. Therefore, in 2007, the angular diameter of the emitting region is larger than that in 2011 by a factor of ≈ 6 , which is identical to the observed change in the flux between the two epochs.

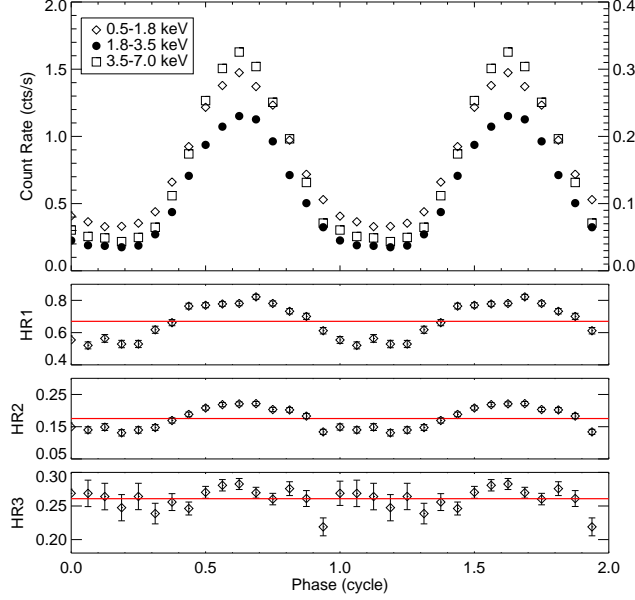


Fig. 4.— Pulse profile and its energy dependence during the 2011 observation. Figure labels and symbols are the same as in Figure 3.

Table 3. Results of the phased resolved spectroscopic analysis of the 2007 observation.

Phase	N_{H}^1 (10^{22}cm^{-2})	kT (keV)	B (10^{14} G)	β^1	τ^1	Flux ² (dof)	χ^2_{ν}
Peak	$0.80^{+0.01}_{-0.02}$	$0.439^{+0.003}_{-0.010}$	$2.05^{+0.06}_{-0.04}$	0.300 ± 0.005	4.86 ± 0.17	$6.78^{+0.07}_{-0.03}$	1.0708 (477)
Decay	–	$0.399^{+0.003}_{-0.049}$	$1.80^{+0.08}_{-0.13}$	–	–	$4.67^{+0.06}_{-0.03}$	–
Rise	–	$0.410^{+0.043}_{-0.040}$	$1.48^{+0.09}_{-0.07}$	–	–	$5.63^{+0.07}_{-0.09}$	–
Minimum	–	$0.335^{+0.020}_{-0.013}$	$1.73^{+0.08}_{-0.07}$	–	–	$3.12^{+0.04}_{-0.05}$	–

¹ Best-fit values were obtained by linking the parameters over all spin phase intervals.

² Unabsorbed 0.5–7.0 keV flux in units of $10^{-11} \text{erg s}^{-1} \text{cm}^{-2}$.

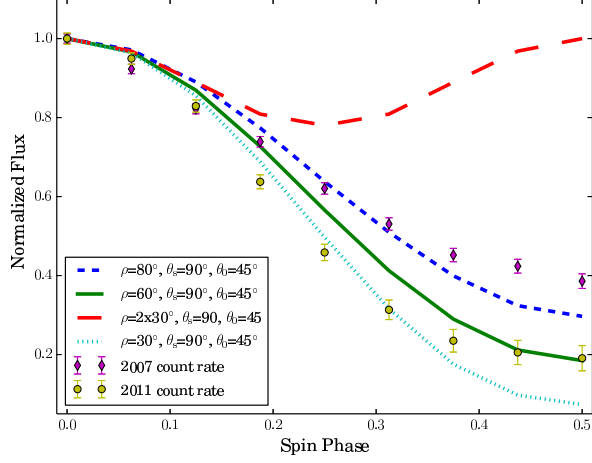


Fig. 5.— Pulse profiles obtained from the two observations in the 0.5–7.0 keV band are shown with purple diamonds (Obs1) and yellow circles (Obs2). The dotted, solid and dashed lines show the theoretically expected pulse profiles with spot sizes of 30° , 60° , and 80° . The long dashed line shows the case for two antipodal spots on the surface each with size of 30° . In order to easily compare the profiles, all the curves are normalized to the flux at the peak and the peak phase is moved to phase 0.0. The plot only extends up to phase 0.5 since the model assumes a symmetric emitting region.

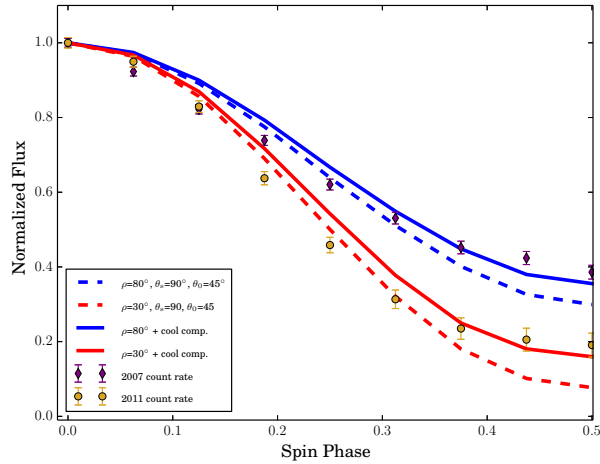


Fig. 6.— Model pulse profiles obtained for the 80° (blue solid line) and 30° (red solid line) hot spots described in Figure 5 but with the addition of an antipodal cool component that has a temperature of 0.2 keV and 0.15 keV, respectively. For comparison, the dashed lines show the models with only one hot spot, with parameters as in Figure 5. Observed 0.5–7.0 keV pulse profiles are shown with purple diamonds (Obs1) and yellow circles (Obs2).

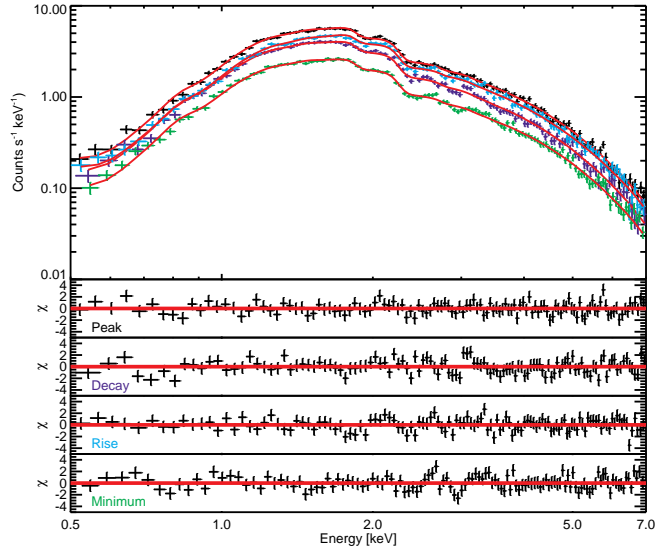


Fig. 7.— Upper panel shows the best fit models to each data set at different spin phase intervals. Lower panels show the residuals from the best fit models for individual spin phases.

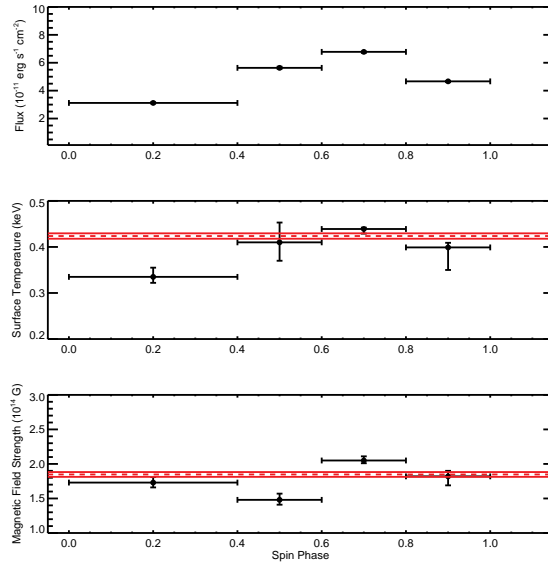


Fig. 8.— Evolution of the 0.5–7.0 keV unabsorbed flux, the surface temperature and the magnetic field strength of the hot region on the surface as a function of neutron star spin phase. Red dashed and solid lines show the error weighted averages of the individual best fit values and their $1-\sigma$ uncertainties.

This suggests that after the timing glitch observed in 2007, the size of the hot spot on the neutron star surface changed, increasing to about 80° and causing the observed increase in the X-ray flux. By 2011, it returned close to its pre-burst, quiescent level of 30° .

If a single rotating hot spot described by one temperature captures the physical conditions relevant for the surface of 1E 1048.1–5937, then we expect to only see insignificant differences in the surface temperatures obtained from the phase-resolved spectra that are consistent within statistical uncertainties. For the peak, rise, and decay phases, this is indeed what we obtain: the standard deviation of the best fit temperature for these phases is equal to the formal uncertainties of the individual measurements (see Figure 8), indicating that a single rotating hot spot with an angular size of $\approx 80^\circ$ dominates the observed flux during these spin phases. This model, however, does not adequately account for the flux in the phase minimum as shown in Figure 5, where the rest of the surface, albeit being much cooler, is expected to contribute to the emission. We showed in Section 4.2 and Figure 6 that adding the contribution from such a cool component that is 180° out-of-phase with the hot spot indeed leads to a better description of the profile at the pulse minimum. This component will naturally introduce a small modification to the spectral parameters obtained from the fits at the pulse minimum and may account for the discrepancy between the temperatures at the phase minimum and the other three phases. Testing this hypothesis is beyond the computational capabilities of our current setup.

We compare the magnetic field strengths we derived here with other independently obtained estimates of the field in this source. We obtained an average magnetic field strength of 1.8×10^{14} G, covering a range from 1.48 to 2.05×10^{14} G at different pulse phases, which is a scatter at the 2σ -level given the statistical uncertainties in each of these measurements. In an earlier study where we applied the STEMS model to the phase-averaged spectrum obtained from the 2003 XMM-Newton observation of this source, we reported an average field strength of $(2.26 \pm 0.05) \times 10^{14}$ G (Özel, Güver, & Göğüş 2008), which is similar to the present findings. The small difference is caused by the fact that general relativistic transport was applied to the average spectrum as a whole in this earlier study rather than to spectra at each pulse phase; this introduces a difference in the spectrum observed at infinity when the emerging radiation is highly beamed. There are naturally other sources of systematic uncertainty or bias arising from our assumption of constant magnetic field strength and direction throughout the polar cap and in the magnetosphere. In the absence of first-principles calculations of the magnetic field topology and the strength of the currents in the magnetosphere, it is difficult to predict the direction of this bias. However, the close similarity between the magnetic fields inferred from pulse-phase averaged spectra and those of the individual pulse phases suggests that the geometric effects such as those we neglected here do not change the results substantially. An estimate of the dipole magnetic field strength can also be obtained from the rate of spindown in pulsars. 1E 1048.1–5937 has a spin period of 6.452 s, with a period derivative that shows large excursions in the range $\dot{P} = (0.86 - 3.81) \times 10^{-11} \text{ss}^{-1}$ (Kaspi et al. 2001). Using the standard magnetic dipole radiation formula, the range of magnetic field strengths implied by these measurements is $B_{\text{dip}} = (2.4 - 4) \times 10^{14}$ G, where we assumed a neutron star radius

of $R = 10$ km and a moment of inertia of $I = 10^{45}$ g cm². This shows a reasonable agreement between the field strengths obtained from spectral and timing methods.

Finally, we combine the surface areas we obtain from pulse profile modeling and phase resolved spectroscopy with previously reported values of the pulsed fraction of 1E 1048.1–5937 at different epochs to reconstruct a physical picture of its recent activity. Tam et al. (2008) reported a 2–10 keV RMS pulsed fraction of $\approx 70\%$ for 1E 1048.1–5937, using several Chandra observations throughout 2006 when the source showed no activity. In March 2007, 1E 1048.1–5937 showed a pulsed flux increase, which was followed by a spin-up glitch (Dib et al. 2009). Subsequent observations with imaging X-ray telescopes revealed that the total flux increased by a factor of ≈ 7 , while the pulsed fraction decreased significantly from $\approx 70\%$ to $\approx 30\%$ (Tam et al. 2008). The observed anti-correlation between the total flux and the pulsed fraction was attributed to a growing hot spot on the neutron star surface (Tam et al. 2008; see Özel & Güver 2007). Our findings support this hypothesis. We measured a pulsed fraction of 35% in the 2–10 keV band as well as a spot size of $\approx 80^\circ$ in the 2007 observation, which was performed approximately 3 months after the onset of the glitch event (Dib et al. 2009). The pulsed fraction is still significantly lower than that before the flux increase but shows that the neutron star was already recovering after the 2007 event. In 2011, we observe that the pulsed fraction returned to $\approx 65\%$ level while the size of the hot spot decreased to $\approx 30^\circ$. These results suggest that the emitting area grows significantly during flares and glitches but recovers back to its persistent and significantly smaller size within a few year timescale.

Acknowledgments

We thank the anonymous referee for his/her detailed comments and suggestions. TG acknowledges support from the Scientific and Technological Research Council of Turkey (TÜBİTAK BİDEB) through a fellowship programme. F.Ö. gratefully acknowledges support from NSF grant AST-1108753.

REFERENCES

- Albano, A., Turolla, R., Israel, G. L., et al. 2010, *ApJ*, 722, 788
- An, H., Kaspi, V. M., Archibald, R., & Cumming, A. 2013, *ApJ*, 763, 82
- Anders, E., & Ebihara, M. 1982, *Geochim. Cosmochim. Acta*, 46, 2363
- Arnaud, K. A. 1996, *Astronomical Data Analysis Software and Systems V*, 101, 17
- Bernardini, F., Perna, R., Gotthelf, E. V., et al. 2011, *MNRAS*, 418, 638
- Buccheri, R., Bennett, K., Bignami, G. F., et al. 1983, *A&A*, 128, 245

- Dib, R., Kaspi, V. M., & Gavriil, F. P. 2009, *ApJ*, 702, 614
- Durant M., van Kerkwijk M. H., 2006, *ApJ*, 650, 1070
- Fernández, R., & Thompson, C. 2007, *ApJ*, 660, 615
- Gavriil, F. P., Kaspi, V. M., & Woods, P. M. 2002, *Nature*, 419, 142
- Gavriil, F. P., & Kaspi, V. M. 2002, *ApJ*, 567, 1067
- Gavriil, F. P., & Kaspi, V. M. 2004, *ApJ*, 609, L67
- Gavriil, F. P., Kaspi, V. M., & Woods, P. M. 2006, *ApJ*, 641, 418
- Güver, T., Özel, F., Göğüş, E., & Kouveliotou, C. 2007, *ApJ*, 667, L73
- Güver, T., Özel, F., Göğüş, E. 2008, *ApJ*, 675, 1499
- Güver, T., Göğüş, E., Özel, F. 2011, *MNRAS*, 418, 2773
- Ho, W. C. G., & Lai, D. 2001, *MNRAS*, 327, 1081
- Ho, W. C. G., Lai, D., Potekhin, A. Y., & Chabrier, G. 2003, *ApJ*, 599, 1293
- Ho, W. C. G., & Lai, D. 2003, *MNRAS*, 338, 233
- Kaspi, V. M., Gavriil, F. P., Chakrabarty, D., Lackey, J. R., & Muno, M. P. 2001, *ApJ*, 558, 253
- Kaspi, V. M. 2007, *Ap&SS*, 308, 1
- Lloyd, D. A. 2003, *arXiv:astro-ph/0303561*
- Lyutikov, M., & Gavriil, F. P. 2006, *MNRAS*, 368, 690
- Mereghetti, S. 2008, *A&A Rev.*, 15, 225
- Ng, C.-Y., Kaspi, V. M., Dib, R., et al. 2011, *ApJ*, 729, 131
- Nobili, L., Turolla, R., & Zane, S. 2008, *MNRAS*, 386, 1527
- Oosterbroek, T., Parmar, A. N., Mereghetti, S., & Israel, G. L. 1998, *A&A*, 334, 925
- Olausen, S. A., & Kaspi, V. M. 2014, *ApJS*, 212, 6
- Özel, F. 2001, *ApJ*, 563, 276
- Özel, F. 2002, *ApJ*, 575, 397
- Özel, F. 2003, *ApJ*, 583, 402
- Özel, F. 2013, *Reports on Progress in Physics*, 76, 016901

- Özel, F., Güver, T. 2007, *ApJ*, 659, L141
- Özel, F., Güver, T., Göğüş, E. 2008, 40 Years of Pulsars: Millisecond Pulsars, Magnetars and More, 983, 254
- Özel, F., Psaltis, D., & Kaspi, V. M. 2001, *ApJ*, 563, 255
- Pechenick, K. R., Ftaclas, C., & Cohen, J. M. 1983, *ApJ*, 274, 846
- Poutanen J., Beloborodov A. M., 2006, *MNRAS*, 373, 836
- Psaltis, D., Özel, F., & DeDeo, S. 2000, *ApJ*, 544, 390
- Rea, N., Zane, S., Turolla, R., Lyutikov, M., Götz, D. 2008, *ApJ*, 686, 1245
- Rea, N., Esposito, P., Turolla, R., et al. 2010, *Science*, 330, 944
- Rea, N., & Esposito, P. 2011, High-Energy Emission from Pulsars and their Systems, 247
- Rea, N., Israel, G. L., Esposito, P., et al. 2012, *ApJ*, 754, 27
- Rea, N., Viganò, D., Israel, G. L., Pons, J. A., & Torres, D. F. 2014, *ApJ*, 781, L17
- Tam, C. R., Gavriil, F. P., Dib, R., et al. 2008, *ApJ*, 677, 503
- Thompson, C., & Duncan, R. C. 1995, *MNRAS*, 275, 255
- Thompson, C., Lyutikov, M., & Kulkarni, S. R. 2002, *ApJ*, 574, 332
- Tiengo, A., Göhler, E., Staubert, R., & Mereghetti, S. 2002, *A&A*, 383, 182
- Tiengo, A., Mereghetti, S., Turolla, R., et al. 2005, *A&A*, 437, 997
- Tiengo, A., Esposito, P., Mereghetti, S., et al. 2013, *Nature*, 500, 312
- Seward, F. D., & Chlebowski, T. 1982, *ApJ*, 256, 530
- Seward, F. D., Charles, P. A., & Smale, A. P. 1986, *ApJ*, 305, 814
- Scholz, P., & Kaspi, V. M. 2011, *ApJ*, 739, 94
- van der Klis, M. 1989, in *Timing Neutron Stars*, ed. H. Ögelman & E. P. J. van den Heuvel (Dordrecht: Kluwer), 27
- Woods, P. M., Kaspi, V. M., Thompson, C., et al. 2004, *ApJ*, 605, 378399
- Woods, P. M., & Thompson, C. 2006, Compact stellar X-ray sources, 547
- Zavlin, V. E., Pavlov, G. G., & Shibano, Y. A. 1996, *A&A*, 315, 141

Zavlin, V. E., & Pavlov, G. G. 2002, *Neutron Stars, Pulsars, and Supernova Remnants*, 263

Zhou, P., Chen, Y., Li, X.-D., et al. 2014, *ApJ*, 781, L16